Mem. S.A.It. Vol. 90, 535

Memorie della

[C I] observations toward 49 Ceti with ASTE and ALMA

A. E. Higuchi

National Astronomical Observatory of Japan, Osawa, Mitaka, Tokyo 181-8588, Japan
e-mail: `aya.higuchi@nao.ac.jp`

Abstract. We present the first sub-arcsecond images of 49 Ceti in the [C I] $^3P_1$–$^3P_0$ emission and the 614 μm dust continuum emission observed with the Atacama Large Millimeter/submillimeter Array (ALMA), as well as that in the CO(J=3–2) emission prepared by using the ALMA archival data. This result supported the first detection of [C I] emission from 49 Ceti with the 10 m telescope of the Atacama Submillimeter Telescope Experiment (ASTE). The spatial distribution of the 614 μm dust continuum emission is found to have a broad-ring structure with a radius of about 100 au around the central star. The [C I] emission map shows two peaks inside the dust ring, and its overall extent is comparable to that of the dust continuum emission and the CO emission. We find that the [C I]/CO(J=3–2) intensity ratio significantly varies along the major axis. The ratio takes the minimum value of 1.8 around the dust peak position, and increases inwards and outwards. The enhanced ratio around the central star (∼3) likely originates from the stellar UV radiation, while that in the outer disk (∼10) from the interstellar UV radiation. Such complex distributions of the [C I] and CO(J=3–2) emission will be a key to understand the origin of the gas in 49 Ceti, and will also provide a stringent constraint on physical and chemical models of gaseous debris disks.

Key words. stars: planetary systems, individual (49 Ceti) — planet: debris disks — planet: formation — protoplanetary disks

1. Introduction

Debris disks are optically thin circumstellar dust components around main-sequence stars, and are crucial to our understanding of the formation of planetary bodies, such as planets, comets, and asteroids. Debris disks stand between gas-rich protoplanetary disks and mature planetary systems, and their investigation sheds light on the late stages of planet formation. Almost all the gas in debris disks is thought to have dissipated, and dust grains smaller than 10 μm are therefore expected to be quickly blown out by stellar radiation pressure from the central star (especially at $\geq 10 L_{\odot}$) (e.g., Wyatt 2008). However, recent observational studies at infrared wavelengths have shown that such small grains survive in debris disks (e.g., Ishihara et al. 2017). One possible mechanism by which small grains remain for a long time is that the gas component remains in debris disks to a moderate extent.

Why debris disks can possess a gas component is not well understood. One possibility is that such gas has a primordial origin; i.e., the gas is the remnants of a protoplanetary gas disk. The other possibility is that the gas has a secondary origin, for which several different mechanisms can be considered; e.g., the sublimation of dust grains (Kobayashi et al. 2011) or planetesimals (Lagrange et al. 1998), photo-sputtering of dust grains (Grigorieva et al. 2007), collisional vaporization of dust grains (Czechowski & Mann 2007), and collision of comets or icy planetesimals (Zuckerman & Song 2012). Such secondary gas is thought to be mainly composed of CO and H_2O (Mumma & Charnley 2011), while only a small amount of H_2 is expected.

Several debris disks harboring a gas component have been discovered in survey observations at optical, infrared, and radio wavelengths, and its origin has been discussed in terms of the evolution of protoplanetary disks and the formation of planetary bodies. In fact, many debris disks are known to reveal submillimeter-wave CO emission, e.g., 49 Ceti (Hughes et al. 2017), β Pictoris (Dent et al. 2014), and 15 others or more (e.g., Kóspál et al. 2013; Moór et al. 2013, 2017; Matrà et al. 2017; Hughes et al. 2018). In addition to the CO emission, the submillimeter-wave [C I] emission has been observed toward a few debris disks. For instance, Higuchi et al. (2017) detected the bright [C I] $^3P_1$–$^3P_0$ toward 49 Ceti and β Pictoris with the ASTE 10 m telescope. The [C I] emission has also been observed with ALMA toward β Pictoris (Cataldi et al. 2018) and HD 131835 (Kral et al. 2018). Interestingly, the [C I] intensity is found to be higher than the CO intensity, which contrasts with the protoplanetary disk case (Tsukagoshi et al. 2015; Kama et al. 2016). However, the origin of the strong [C I] emission from debris disks is not well understood.

49 Ceti is a famous A-type star, located at d = 57±0.3 pc (Gaia Collaboration et al. 2018), at the age of 12 – 50 Myr (Zuckerman & Song 2012; Zuckerman 2019). The CO emission was first detected with JCMT (e.g., Zuckerman et al. 1995; Dent et al. 2005), partially resolved with SMA (Hughes et al. 2008), and clearly imaged with ALMA (Hughes et al. 2017; Moór et al. 2019). According to Higuchi et al. (2017), the [C I] line profile resembles that of CO. This result suggests that atomic carbon (C) would coexist with CO in the debris disks, and C is likely formed by the photodissociation of CO. Furthermore, a simple chemical model indicates a small number of H_2 molecules in the gas disk. However, the above interpretation depends on the physical parameters, such as visual extinction and dust size, employed in chemical models, and thus it is necessary to resolve the spatial distribution of the disk in order to understand the effect of UV radiation from the central star and from interstellar space. Although the [C I] emission from β Pictoris (Cataldi et al. 2018) and HD 131835 (Kral et al. 2018) has been imaged with ALMA, a detailed comparison between their CO and [C I] images is difficult due to an insufficient signal to noise ratio of the [C I] data. In this study, we present a high-quality image of 49 Ceti in the [C I] emission observed with ALMA, and report the spatial structure of the [C I] emission at a resolution of $0\farcs5$ (30 au).

2. Observations

2.1. ASTE observations

We observed the [C I] $^3P_1$–$^3P_0$ (492.161 GHz) and CO(J=3–2) (345.796 GHz) lines toward 49 Ceti from September to October 2016 with the 10 m telescope of the Atacama Submillimeter Telescope Experiment (ASTE). An Atacama Large Millimeter/submillimeter Array (ALMA) Band 8 (400–500 GHz) qualification model receiver, Band 8 QM (Satou et al. 2008) and a two-sideband separating receiver, DASH 345, were employed for the [C I] and CO(J=3–2) observations, respectively. The half-power beam width (HPBW) was 17″ (Band 8) and 22″ (DASH 345), and the main beam efficiency $\eta_{\rm MB}$ was 45% (Band 8) and 60% (DASH 345). As a backend, we used MAC, a 1024-channel digital auto-correlator that has bandwidth of 128 MHz and resolution of 125 kHz. The bandwidth corresponds to 78 and 111 km s^{-1} at 492 and 345 GHz, respectively, while the resolution corresponds to 0.076 and 0.11 km s^{-1} at 492 and 345 GHz, respectively. The position switching method was employed. The OFF positions were taken to be 15 to 30′ away from the stellar positions.

Telescope pointing calibration was performed every 1.5–2 hours by observing O-Cet

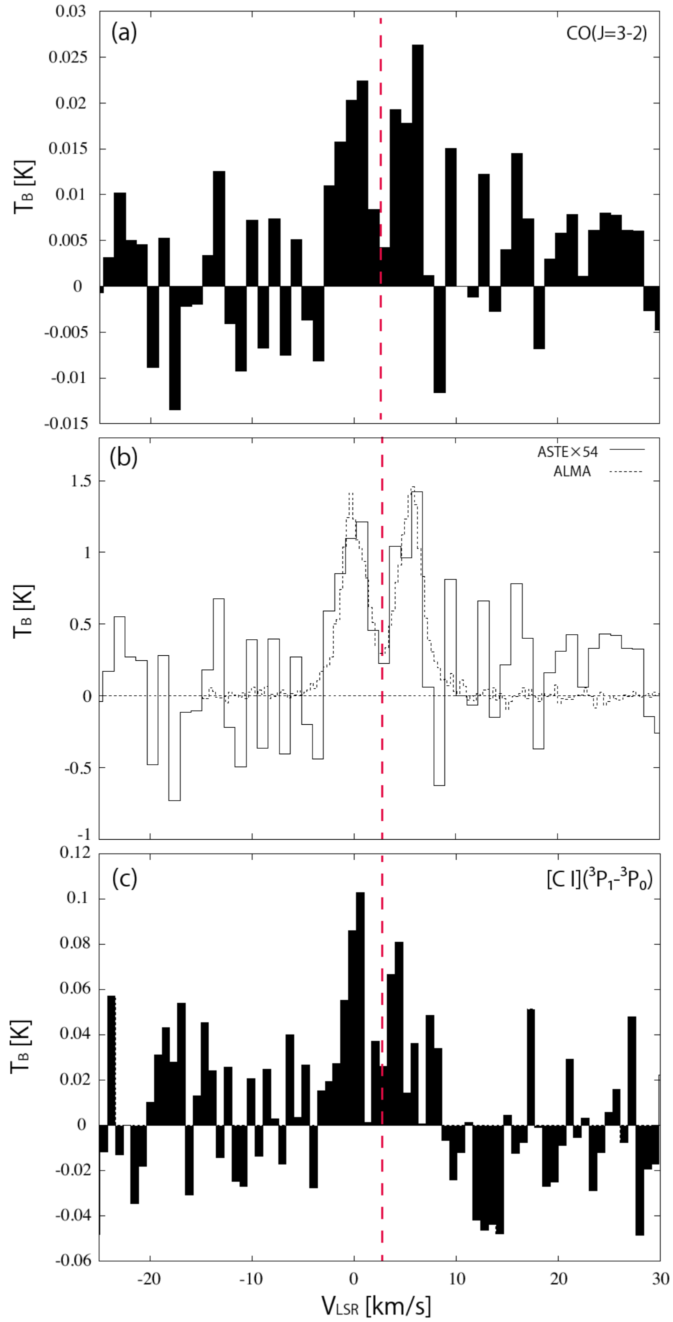

Fig. 1. (a): CO spectrum observed with the ASTE toward 49 Ceti. (b): Comparison with the ALMA spectrum. (c): [C I] spectrum observed with the ASTE toward 49 Ceti. The vertical red line indicates the systemic velocity of the gas disk (Higuchi et al. 2017).

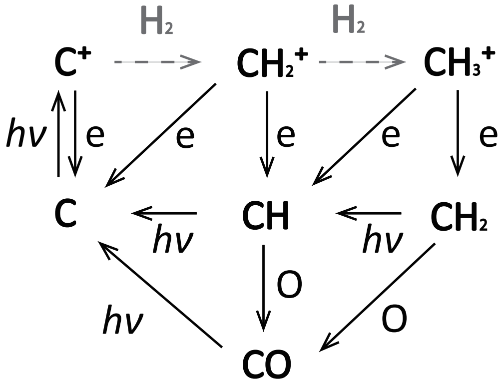

Fig. 2. Basic carbon chemistry producing CO in debris disks (Higuchi et al. 2017).

and IRC+10216 in the CO(J=3–2) emission line, and the resulting pointing accuracy was 2″. The [C I] data were obtained under good sky conditions ($\tau_{220\ \mathrm{GHz}} < 0.05$), whereas the CO($J$=3–2) data were obtained under moderate sky conditions ($\tau_{220\ \mathrm{GHz}} > 0.05$). The system noise temperatures typically ranged from 1000 to 1500 K for [C I] and from 250 to 450 K for CO(J=3–2). The observation data were reduced using the software package NEWSTAR developed by the Nobeyama Radio Observatory.

2.2. ALMA observations

49 Ceti was observed with ALMA during Cycle 5 in its compact configuration by using the Band 8 receivers. The observing condition was excellent, where the precipitable water vapor (PWV) during the observation ranged from 0.19 to 0.81 mm. The observations were done in 7 execution blocks with 43 12-m antennas. The minimum and maximum baseline lengths achieved during the observations were 15 m and 500 m, respectively. On-source integration time was 5.9 hours. The synthesized beam for the 614 μm dust continuum is 0.″51×0.″43 with P.A.= − 84.8°, while that for the [C I] $^3P_1$–$^3P_0$ line (492.161 GHz) is 0.″50×0.″42 with P.A.= − 84.8°. At the distance of 49 Ceti (d∼57 pc), the angular size of 0.″5 corresponds to 30 au. In this observation, the atmospheric water line at 183 GHz was simultaneously observed with water vapor radiometers to measure a temporal variation of the water vapor column in each antenna beam, which was used to reduce the atmospheric phase noise. The quasars J2258-2758, J0141-0928, J2253+1608. and J0423-0120 were employed to calibrate amplitude, bandpass, and complex gain fluctuations, depending on the observing schedule.

In addition, we employed the ALMA archival data of the CO(J=3–2) line emission observed toward this source. The synthesized beam for the CO line is 0.″56×0.″45 with P.A.= − 87.2°, which is comparable to those for the 614 μm continuum and the [C I] line. Detailed information of the CO observation is described in Hughes et al. (2017).

Data reduction was performed by using version 5.3.0 of the Common Astronomy Software Applications (CASA) package (McMullin et al. 2007). The 614 μm continuum map was obtained from a combination of all the line-free channels and by using natural weighting. [C I] and CO images were obtained by using natural weighting. The CASA task *tclean* was used to Fourier-transform the visibility data and to deconvolve the dirty images at a velocity interval of 0.10 km s^{-1}. For the [C I] and CO images, the same parameters in *tclean* were used. In this paper, we present results of the 614 μm dust continuum, the [C I] $^3P_1$–$^3P_0$ line emission, and the CO(J=3–2) line emission.

3. Results and discussions

3.1. ASTE observations

The [C I] $^3P_1$–$^3P_0$ emission was detected from 49 Ceti with ASTE, which was the first detection of such emissions. The line profile of [C I] was found to resemble that of CO(J=3–2) observed with the same telescope and the Atacama Large Millimeter/submillimeter Array (Figure 1) (Higuchi et al. 2017). This result suggests that atomic carbon (C) coexists with CO in the debris disks, and is likely formed by the photodissociation of CO. Assuming an optically thin [C I] emission with the excitation temperature ranging from 30 to

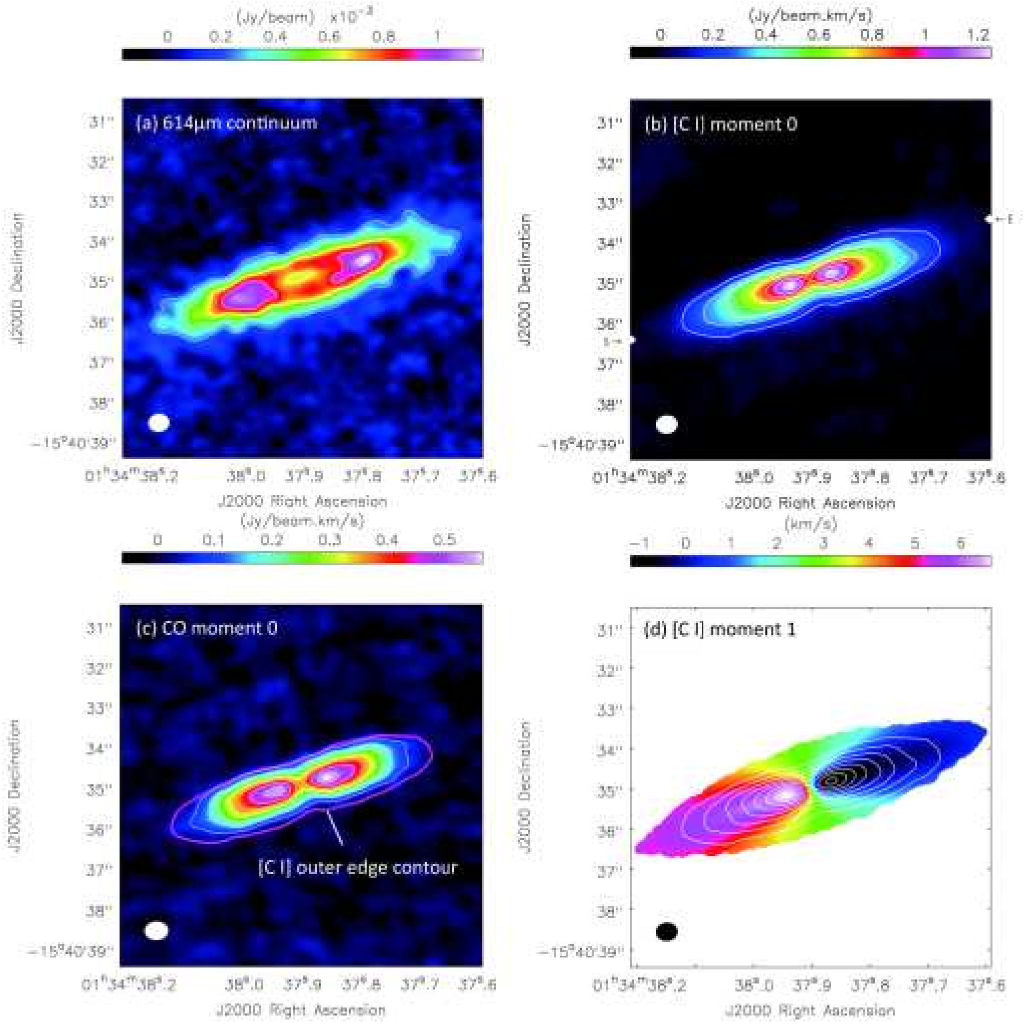

Fig. 3. (a) The 614 μm continuum image. Contours are 5σ, 10σ, 15σ, 20σ, 25σ levels (1σ = 0.045 mJy beam^{-1}). (b) The [C I] integrated intensity map (Velocity range = −6 to 11.5 km s^{-1}). Contours are 5σ, 10σ, 15σ, 20σ, 25σ, 30σ, 35σ, 40σ levels (1σ = 30 mJy beam^{-1} km s^{-1}). The starting (S) and end (E) positions of major axis are indicated. (c) The CO integrated intensity map (Velocity range = −6 to 11.5 km s^{-1}). Contours are 5σ, 10σ, 15σ, 20σ, 25σ, 30σ, 35σ, 40σ levels (1σ = 15 mJy beam^{-1} km s^{-1}). The pink color contour shows the 5σ level of the [C I] integrated intensity map. (d) The [C I] velocity field map. Contours show the [C I] integrated intensity with the same contour level of (b) (Higuchi et al. 2019).

100 K, the column density of C is evaluated to be $(2.2\pm0.2)\times10^{17}$. The C/CO column density ratio is thus derived to be 54±19. This ratio is higher than those of molecular clouds and diffuse clouds by an order of magnitude. The unusually high ratio of C to CO is likely attributed to a lack of H_2 molecules needed to reproduce CO molecules efficiently from C (Figure 2).

3.2. ALMA observations

Figure 3(a) shows the 614 μm dust continuum map at a 0.″5 resolution (Higuchi et al. 2019). The 614 μm continuum emission is distributed to a broad-ring structure around the central star. Figure 3(b) shows the integrated intensity map of the [C I] emission, where the velocity range

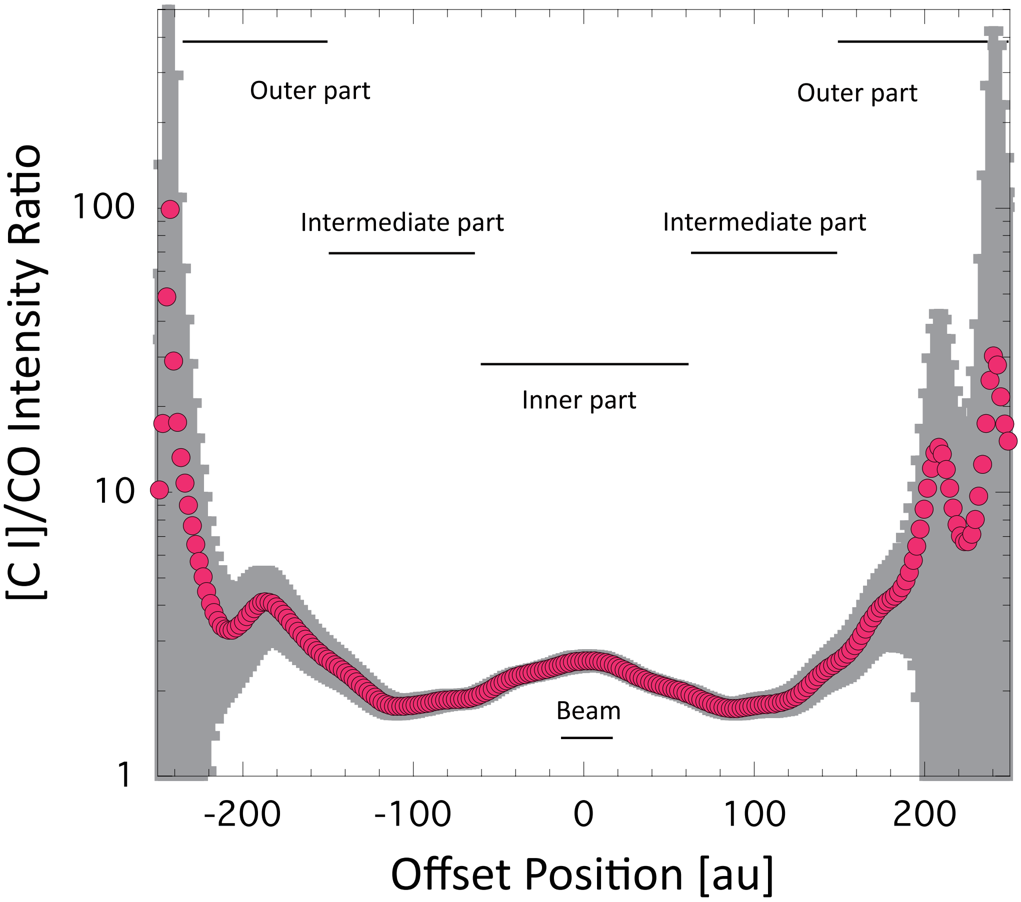

Fig. 4. The [C I]/CO intensity ratio as a function of the projected distance. The gray shaded area shows the error bar that indicates the propagation of the 1 σ rms noise level of the integrated intensity map (Higuchi et al. 2019).

for integration is from −6 to 11.5 km s^{-1}. The [C I] distribution has a double-peaked structure inside the broad ring distribution of the dust continuum emission. Figure 3(c) shows the integrated intensity map of the CO (J=3–2) emission, where the velocity range for integration is from −6 to 11.5 km s^{-1}. The CO distribution also reveals a double-peaked feature inside the dust continuum peak, as in the case of the [C I] emission. An overall extent of the CO emission is similar to that of the [C I] emission. Figure 3(d) shows the velocity field map of the [C I] emission, which clearly show the rotating disk.

Figure 4 depicts the [C I]/CO intensity ratio along the major axis. The ratio has the minimum value around the intermediate region where the dust continuum emission peaks, and increases inwards and outwards. In order to interpret this characteristic variation of the [C I]/CO intensity ratio, we need to evaluate the column densities of C and CO at each offset position from the central star. However, their derivation is not straightforward. Recently, Moór et al. (2019) detected the ^{13}CO(J=2–1) emission as well as the ^{12}CO(J=2–1) emission from 49 Ceti by ALMA ACA (Atacama Compact Array) observation at a resolution of

6″. According to their result, the flux ratio (r) of ^{12}CO(J=2–1)/^{13}CO(J=2–1) is 2.3±0.2. Thus, the optical depth of the ^{12}CO(J=2–1) emission (τ) is derived to as high as be 43±7 by using the result in Moór et al. (2019). The ^{12}CO(J=2–1) line is indeed optically thick. Likewise the CO(J=3–2) line is most likely optically thick as well.

For this reason, the CO mass evaluated from the optically thin ^{13}CO emission (> 0.01 $M_{\oplus}$) is higher by two orders of magnitude than the previous estimate (> 10^{-4} $M_{\oplus}$) (Hughes et al. 2017; Higuchi et al. 2017). Thus, the CO mass in 49 Ceti is higher by three orders of magnitude than the CO mass (3.4×10^{-5} $M_{\oplus}$) in β Pictoris (Dent et al. 2014; Matrà et al. 2017).

We face a similar but more serious situation for the optical depth of the [C I] emission. Considering that the [C I] intensity is comparable to or even higher than the CO intensity, we cannot simply assume the optically thin condition for the [C I] emission. Thus, it is difficult to derive the column densities of CO and C from the observed intensities based on the current dataset. Therefore, we qualitatively discuss the behavior of the characteristic variation of the [C I]/CO intensity ratio in this study.

As shown in Figure 4, the [C I]/CO intensity ratio increases from the intermediate part to the inner and outer parts. This trend can be interpreted as the different variation of the number density of C and CO along the major axis, the different variation of the excitation temperature of the [C I] and CO emission, or the mixture of both.

The C/CO abundance ratio in the gas is mainly determined by the strength of the UV radiation and the amount of H_2 molecules (e.g., Higuchi et al. 2017; Iwasaki et al. 2019). The former controls the dissociation of CO to produce C and C^+, while the latter contributes to the reproduction of CO from C^+. However, the optical depth problem hampers quantitative discussions on the C/CO abundance ratio. For detailed modeling, we need spatially-resolved images of the other transitions of ^{12}CO, ^{13}CO and [C I], which allow us to make a correction for the optical depth effect.

References

Cataldi, G., Brandeker, A., Wu, Y., et al. 2018, ApJ, 861, 72

Czechowski, A., & Mann, I. 2007, ApJ, 660, 1541

Dent, W. R. F., Greaves, J. S., & Coulson, I. M. 2005, MNRAS, 359, 663

Dent, W. R. F., Wyatt, M. C., Roberge, A., et al. 2014, Science, 343, 1490

Dong, R., van der Marel, N., Hashimoto, J., et al. 2017, ApJ, 836, 201

Gaia Collaboration, Brown, A. G. A., Vallenari, A., et al. 2018, A&A, 616, A1

Grigorieva, A., Artymowicz, P., & Thébault, P. 2007, A&A, 461, 537

Higuchi, A. E., Sato, A., Tsukagoshi, T., et al. 2017, ApJ, 839, L14

Higuchi, A. E., Saigo, K., Kobayashi, H., et al. 2019, ApJ, submitted

Holland, W. S., Matthews, B. C., Kennedy, G. M., et al. 2017, MNRAS, 470, 3606

Hughes, A. M., et al. 2008, ApJ, 681, 626

Hughes, A. M., Lieman-Sifry, J., Flaherty, K. M., et al. 2017, ApJ, 839, 86

Hughes, A. M., Duchêne, G., & Matthews, B. C. 2018, ARA&A, 56, 541

Ishihara, D., Takeuchi, N., Kobayashi, H., et al. 2017, A&A, 601, A72

Iwasaki, K., Kobayashi, H., in prep.

Kama, M., Bruderer, S., Carney, M., et al. 2016, A&A, 588, A108

Kobayashi, H., et al. 2011, Earth, Planets, and Space, 63, 1067

Kóspál, Á., Moór, A., Juhász, A., et al. 2013, ApJ, 776, 77

Kral, Q., et al. 2019, MNRAS, 489, 3670

Lagrange, A.-M., Beust, H., Mouillet, D., et al. 1998, A&A, 330, 1091

McMullin, J. P., et al. 2007, Astronomical Data Analysis Software and Systems XVI, 376, 127

Matrà, L., MacGregor, M. A., Kalas, P., et al. 2017, ApJ, 842, 9

Moór, A., Juhász, A., Kóspál, Á., et al. 2013, ApJ, 777, L25

Moór, A., Curé, M., Kóspál, Á., et al. 2017, ApJ, 849, 123

Moór, A., Kral, Q., Ábrahám, P., et al. 2019, ApJ, submitted

Mumma, M. J., & Charnley, S. B. 2011, ARA&A, 49, 471
Roberge, A., Kamp, I., Montesinos, B., et al. 2013, ApJ, 771, 69
Satou, N., Sekimoto, Y., Iizuka, Y., et al. 2008, PASJ, 60, 1199
Tsukagoshi, T., Momose, M., Saito, M., et al. 2015, ApJ, 802, L7
Wyatt, M. C. 2008, ARA&A, 46, 339
Zuckerman, B., Kim, S. S., & Liu, T. 1995, ApJ, 446, L79
Zuckerman, B., & Song, I. 2012, ApJ, 758, 77
Zuckerman, B. 2019, ApJ, 870, 27